Phase field parameters for battery compounds from first-principles calculations

Nicolas G. Hörmann[1,2] and A. Groß[2,3]

[1]*Theory and Simulation of Materials (THEOS), and National Centre for Computational Design and Discovery of Novel Materials (MARVEL), École Polytechnique Fédérale de Lausanne, 1015 Lausanne, Switzerland*

[2]*Helmholtz Institute Ulm (HIU) Electrochemical Energy Storage, Albert-Einstein-Allee 11, 89069 Ulm, Germany*

[3]*Universität Ulm, Institut für Theoretische Chemie, Albert-Einstein-Allee 11, 89069 Ulm, Germany*

(Received 29 January 2019; published 13 May 2019)

In this work, we present and apply schemes to determine from first-principles calculations the relevant effective parameters used in phase field theory simulations of battery compounds. In particular, we derive that a consistent free energy density can be obtained by mean-field sampling, which is especially suited for materials with different configurations on a lattice, such as alloys or Li intercalation batteries. In addition, it is demonstrated that mean-field sampling can be performed very effectively with the use of special quasi random structures and that experimentally determined free energy density parameters for $LiFePO_4$ are reproduced by density functional theory calculations. The additional computation of interfacial and strain energy parameters allows us to present a consistent phase field parametrization of Li_2FeSiO_4 without relying on experimental data.

DOI: 10.1103/PhysRevMaterials.3.055401

I. INTRODUCTION

The thermodynamics of many solids can be understood from lattice based models such as the Ising model or its generalization in form of the cluster expansion [1]. Such lattice-based models are used more and more in material science to simulate relevant materials properties such as, e.g., the phase diagram of alloys or Li batteries, as they allow efficient sampling of configuration space and numerical solution of statistical mechanics integrals [2–6]. On the other hand, the time- and length scales of many relevant phenomena, as, e.g., microstructure evolution or nucleation and growth, are out of reach for atomistic sampling methods, such that coarse-grained continuum models as, e.g., phase field models [7–12] are necessary.

In the case of Li-ion batteries, many important properties like phase stability, open circuit voltages or migration barriers and equilibrium (dis-)charge profiles can be understood from first-principles calculations [13,14]. However, several aspects of kinetics are less understood, especially for phase-separating intercalation materials, where metastable phases and strain effects can become important [15–22]. In this case, it is necessary to include knowledge from continuum scale simulations, e.g., via phase field models [11,23–26] in order to get a full understanding of electrode behavior which depends on single particle properties. Furthermore, this also allows to address the collective behavior of the many interconnected particles which the electrode consists of [4,27–30].

A central part of phase field models is the energy density functional, a very basic one being the Cahn-Hilliard energy functional [31,32], which defines the free energy as

$$\Phi[x(\mathbf{r})] = \int_V [\phi(x(\mathbf{r}), T) + \kappa(\nabla x)^2]\rho dV. \tag{1}$$

In the case of a phase-separating material with stable low- and high-concentration phases, ρ would correspond to a site density, $x(\mathbf{r})$ to a normalized, local concentration, $\phi(x(\mathbf{r}), T)$ to the (nonconvex) local free energy density and $\kappa(\nabla x)^2$ to gradient corrections, which contribute, e.g., to interface energies. It can be viewed as local density plus gradient approximation within a classical density functional theory framework [33]. Many important properties, e.g., the spinodal points, depend on the nonconvex shape of $\phi(x)$. In the case of Li batteries, the basic functional of Eq. (1) is typically augmented with anisotropic interfacial terms and strain and surfaces contributions [23–26,34–39].

Furthermore, it has been realized that an important step towards making phase field models predictive is to use consistent parameter sets, which is typically done by combining experimental data [23–26] or CALPHAD [40,41] modeling results [42–46] with theoretical insights, e.g., for interface or elastic terms. To our knowledge, a consistent and efficient approach to derive phase field parameters from pure *ab initio* calculations is still missing.

In this work, we propose and test three consistent construction schemes for the non-convex homogeneous free energy density $\phi(x)$ of phase-separating compounds based on ab-initio calculations and mean-field theory. The schemes are efficient and generally applicable also in other fields of material science, e.g., for approximating phase diagrams.

Experimentally determined continuum parameters for $LiFePO_4$ (LFP) are reproduced purely based on density functional theory (DFT) calculations. Afterwards, we determine the corresponding parameters for $Pmn2_1$ Li_2FeSiO_4 (LFS)—a cheap and promising cathode material for future Li ion batteries [47–52]. To our knowledge, there are neither theoretical nor experimental continuum parameters available to date for this material. Therefore, we also determine the interface energy and strain energy parameters, that are typically used in phase field simulations of phase-separating Li intercalation compounds from DFT calculations for LFS.

With this study we try to contribute to the understanding of phase-separating battery materials in particular, as it will open the pathway towards understanding the different behavior of Li_2FeSiO_4 and $LiFePO_4$ from a continuum scale perspective. The methodological recipe for the determination of phase field parameters, however, is general and can be applied equally, e.g., to alloy systems.

II. DENSITY FUNCTIONAL THEORY CALCULATIONS

This paper relies on density functional theory (DFT) calculations of bulk, defect and interface energies as well as of elastic properties of Li_xFeSiO_4 ($x = 0, \ldots, 2$). Total energies are readily obtained by spin-polarized calculations using the periodic DFT code VASP [53,54] and projector augmented-wave (PAW) pseudopotentials [55,56] with the VASP standards for Li, Fe, and Si and the soft variant for O atoms to reduce the necessary plane-wave cutoff to 400 eV. Brillouin zone integrations were performed on a $3 \times 3 \times 3$ Monkhorst-Pack k-point grid for the $2 \times 2 \times 2$ bulk supercells [16 formular units (f.u.)], similar as in earlier publications [52,57], using Gaussian smearing. As exchange correlation functional, we used the generalized gradient approximation (GGA) of Perdew-Burke-Ernzerhof (PBE) [58] with Hubbard+U correction for the Fe $3d$ states in the rotationally invariant form [59]. The effective U parameter was set to 4 eV, consistent with previous studies [51,52,57,60,61].

Convergence tests yielded an accuracy of ≈3 meV/f.u. for relative energies. The magnetic orientations of the high spin Fe atoms do not play a major role for this material, which is why we always initialize ferromagnetic-like polarized moments. Geometric relaxations were performed until forces were smaller than 0.01 eV/Å. k-point grids were scaled appropriately for differently sized computational cells, e.g., for interface, surface or strain calculations.

Interface energies between $x = 0$ and 1 phases were determined by performing bulk calculations on periodic solid-solid heterostructures. We chose heterostructures for low index interfaces with a typical cell size of 6 Å × 5 Å × 40 Å, corresponding to two 20-Å-thick single-phase regions as previous surface energy calculations showed that even such drastic changes in the chemical environment as experienced at surfaces decay approx. ≈7 Å below the surface. In order to treat all interface directions on the same footing, we chose to construct heterostructures starting from the primitive unit cells of the materials Li_1FeSiO_4 and Li_2FeSiO_4 at the common lattice constants of Li_2FeSiO_4. The construction scheme for interfaces and the corrections necessary to treat strain relaxation effects are discussed in the Supplemental Material [63]. We estimate the accuracy of interface energies of our approach to be ≈1 meV/Å^2.

III. METHODOLOGY AND RESULTS

Li extraction of the first Li ion per formula unit (f.u.) from $Pmn2_1$ Li_2FeSiO_4 (LFS) occurs via a two-phase reaction, related to the growth of a Li poor phase at the cost of a Li rich phase [47,48], where they correspond to the stoichiometric compounds Li_2FeSiO_4 and Li_1FeSiO_4 at 0 K. Deintercalation of the second Li per f.u., however, implies extraction voltages beyond the stability window of common electrolytes and structural instabilities [61,62].

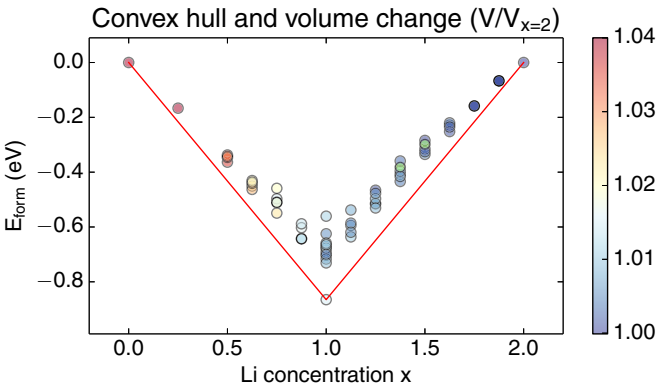

FIG. 1. Formation energies E_{form} for 70 configurations. The values are normalized to the formation enthalpies of Li_2FeSiO_4 and $FeSiO_4$. The convex hull is drawn in red. Relative volumes $V/V_{x=2}$ are visualized according to the color scale at the right-hand side. Green data points exhibit a volume decrease.

Therefore we focus here on the extraction of the first Li per f.u.. We relate the two stable 0 K $Pmn2_1$ $Li_{1+x}FeSiO_4$ phases to Li concentrations $x = 0$, 1 on a sublattice.

On a continuum level, phase separation is characterized by a nonconvex homogeneous bulk free energy $f(x, T)$ or the connected generalized Landau free energy $\phi(x, T, \mu) = f(x, T) - \mu x$, where μ is the imposed Li chemical potential, which can be controlled by the external voltage. (Meta-)stable states are characterized by the minima of ϕ with respect to x:

$$\frac{\partial \phi(x, T, \mu)}{\partial x} = 0. \tag{2}$$

A. Relevant degrees of freedom

In general, the free energy can be derived from the partition function of the systems by appropriate summation over states α. In the case of Li intercalation batteries and other systems that can be mapped onto a lattice the relevant degrees of freedom are the occupancies of lattice sites. It has been shown for $LiFePO_4$ that the electronic degrees of freedom, in form of localized small polarons [64,65], need to be included to derive an accurate phase diagram and solubility limits [66]. In order to test whether localized polarons exist as well in LFS, we analysed the properties of Fe atoms in LFS.

A $2 \times 1 \times 2$ supercell containing eight formula units ($\leqslant$ 64 atoms, $\leqslant$ 16 Li atoms) was studied and Li ions randomly removed for different overall Li concentrations.

The resulting formation energies E_{form} are plotted in Fig. 1, relative to the formation enthalpies of Li_2FeSiO_4 ($x = 2$) and $FeSiO_4$ ($x = 0$). The convex hull (drawn in red) only comprises the three ground states at $x = 2$, 1, and 0, which is indicative for the phase separating properties of LFS. In addition to the stabilities, the illustration also allows to analyze the relative volume changes upon delithiation, which is coded into the color. Between $x = 2$ and $x = 1$ the relative volume change stays limited to below ≈2%, for smaller concentrations, however, considerable volume increase can be observed.

TABLE I. Properties of Fe atoms determined from the stable ground state structures of Li_xFeSiO_4 at $x = 2, 1, 0$. As all Fe atoms are equivalent in these structures the standard deviations are smaller than 10^{-5}, thus not measurable on the presented scale.

x	oxidation state	$3d$ charge (e)	mag. moment (μ_B)	Fe-O bond length (Å)
2	Fe^{2+}	6.097	3.718	2.045
1	Fe^{3+}	5.854	4.216	1.903
0	Fe^{4+}	5.938	3.786	1.822

We studied the properties of the Fe species in all configurations by analyzing the integrated projected valence charge density of Fe $3d$ states, Fe magnetic moments and the average Fe-O bond length of the Fe-O tetrahedra. The existence of integer oxidation states and localized polaronic states should be reflected in discrete, noncontinuous changes in these properties. In Table I, we have listed properties of the three stable groundstate structures with assumed oxidation states 2+, 3+, and 4+. An important property of the three ground states in the convex hull is the equivalence of all Fe atoms which makes the standard deviations for charge, magnetic moment and bond length negligibly small ($<10^{-5}$). The Fe ion properties are plotted for the whole dataset in Fig. 2. The two states Fe^{2+} and Fe^{3+} form clearly separated clusters. However, the Fe^{3+} cluster is connected to the Fe^{4+} state. This confirms that only Fe^{2+} and Fe^{3+} are present for $x = 1, \ldots, 2$, however, for $x < 1$, intermediate states appear (see Fig. 2).

As a result, Fe^{2+} and Fe^{3+} states can be assigned unambigously using a bond-length based classifier (threshold 1.97 Å), where oxidation states 3+ are obtained for smaller Fe-O bond lengths and 2+ for larger ones. In this case, the number of Fe^{3+} ions is found to correspond exactly to the number of removed Li (see Fig. 3).

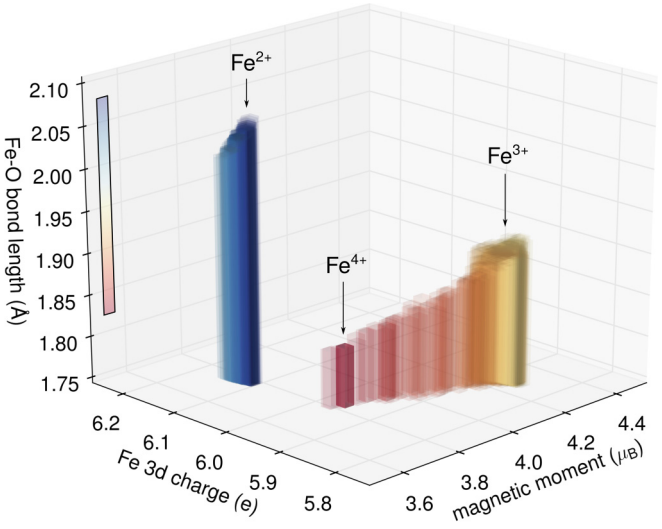

FIG. 2. Fe charge, magnetic moment and Fe-O bond-lengths for all analyzed Fe atoms. The bars are color-coded according to the bond length and semitransparent to visualize the density. The arrows indicate 2+, 3+, and 4+ states.

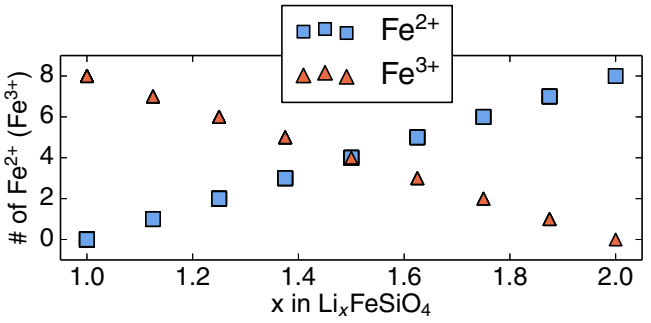

FIG. 3. Number of Fe^{2+} and Fe^{3+} ions for concentrations $x = 1, \ldots, 2$. A bond-length-based classifier was used separating the both oxidation states at a critical Fe-O distance of 1.97 Å.

B. Continuum free energy construction

As in the CALPHAD approach [40,41] and other semiempirical construction schemes of free energies [67], we use an ideal-mixing-like entropy part for the homogeneous free energy. The findings presented above indicate, however, that also the configurational degrees of freedom for Fe^{2+} and Fe^{3+} (small polarons) need to be taken into account appropriately for LFS. This suggests to construct a homogeneous bulk free energy expression by doubling the configurational entropy contributions per f.u. for $Li_{1+x}FeSiO_4$, $x \in [0, 1]$ via

$$f(x, T) = u(x) + 2k_B T[x \ln(x) + (1 - x) \ln(1 - x)]. \quad (3)$$

Taking the 0-K equilibrium Li chemical potential μ_{eq} as a reference such that $\mu = \mu_{eq} + \delta\mu$ the generalized free energy ϕ leads to

$$\phi(x, T, \delta\mu) = \tilde{u}(x) - \delta\mu x + 2k_B T[x \ln(x) + (1 - x) \ln(1 - x)], \quad (4)$$

where $\tilde{u}$ corresponds to the homogeneous bulk internal energy above hull. We will restrict ourselves to the following polynomial expression for $\tilde{u}$:

$$\tilde{u}(x) = -(\bar{E}_d + \delta)x(x - 1) + \frac{\delta}{2}x(x^3 - 1). \quad (5)$$

This expression ensures that $\tilde{u}(0) = \tilde{u}(1) = 0$ at the equilibrium chemical potential at 0 K is fulfilled. Note that most phase field theory simulations rely on an even simpler expression for the internal energy with $\delta = 0$ in Eq. (5). We have introduced the additional term with δ to allow for different absolute slopes of $\tilde{u}(x)$ at $x = 0$ and 1, as motivated in the next paragraph.

We note in passing that the real decomposition in internal and entropic contributions of the free energy obtained from appropriate thermodynamic averages might be rather different than given by the semiempirical formula in Eq. (3). The general use of this type of expression in phase field theory indicates, however, that an corresponding construction protocol might be of interest. This is in particular true, as the nonconvex nature of $f(x, T)$ for phase-separating materials cannot be obtained from free energy sampling, as size-converged, free energy sampling leads necessarily to convex free energy landscapes (phase separated states). Here, we propose three different construction schemes of $\tilde{u}$, consistent

with the expression (4): (i) is rather empirical but instructive, (ii) and (iii) are computationally more expensive but formally better defined as they provide the exact mean-field free energy. Descriptions are given specifically for Li intercalation materials, the translation to the field of alloys and related lattice systems is, however, straight-forward.

(i) Defect energies. The first construction scheme for $\tilde{u}$ in Eq. (5) is based on the fact that the change in $\tilde{u}(x)$ for small concentration deviations ϵ from $x = 0$ and 1 is related to a concentration ϵ of "defects" where E_d^0 is the defect energy of a Li interstitial that occupies an empty sublattice sites close to $x = 0$ and E_d^1 the Li vacancies energy within the $x = 1$ phase, respectively. Thus the parameters of Eq. (5) can be related to these defect energies, namely $\bar{E}_d = \frac{E_d^0 + E_d^1}{2}$ and $\delta = E_d^0 - E_d^1$ for 0-K defect energies at the equilibrium chemical potential μ_{eq}.

(ii)+(iii) Homogeneous sampling. Equation (4) can be derived more formally based on mean-field theory. We consider only the configurational degrees of freedom on the sublattice for potential Li sites. In this case, any configuration $\boldsymbol{\sigma}$ can be defined by the site occupancy variables σ_i with values $\sigma_i = 0$ (unoccupied) and 1 (occupied) for site i. The internal energy $U(\boldsymbol{\sigma})$ is a function of the configuration $\boldsymbol{\sigma}$ and could, e.g., be expressed by a cluster expansion.

The free energy for such a Hamiltonian on a lattice can be determined analytically within mean-field theory, e.g., using the ideas of the Bragg-Williams method [68,69] for arbitrary internal energy $U(\boldsymbol{\sigma})$. It is obtained by sampling the system with uncorrelated site occupancy probabilities p_x according to

$$p_x(\sigma_i) = \begin{cases} 1 - x & \text{for } \sigma_i = 0 \\ x & \text{for } \sigma_i = 1 \end{cases}, \tag{6}$$

$$p_x(\boldsymbol{\sigma}) = \prod_i p_x(\sigma_i), \tag{7}$$

$$\langle \hat{O} \rangle_x = \sum_{\boldsymbol{\sigma}} p_x(\boldsymbol{\sigma}) O(\boldsymbol{\sigma}). \tag{8}$$

Here, $O(\boldsymbol{\sigma})$ represents any operator, or observable, and $\langle \hat{O} \rangle_x$ is the corresponding mean-field thermodynamic average given an average concentration x. The mean-field Landau free energy $\phi(x, T, \delta\mu)$ per site is given by

$$\phi(x, T, \delta\mu) = \frac{1}{N} \langle U \rangle_x - \delta\mu \langle \hat{\sigma}_i \rangle_x - \frac{T}{N} \langle S \rangle_x. \tag{9}$$

The probabilities as defined in Eq. (7) can be thought of as a trial grand canonical density matrix and equilibrium solutions found by minimization of the parametric Landau free energy per site $\phi(x, T, \delta\mu)$ with respect to x, in line with Eq. (2).

The average Li concentration per site is $\langle \hat{\sigma}_i \rangle_x = 1 \cdot p_x(\sigma_i = 1) = x$. The resulting configurational entropy per site i is given by

$$\langle s \rangle_x = \frac{\langle S \rangle_x}{N} = \frac{-k_{\text{B}}}{N} \langle \ln \prod_i \hat{p}_i \rangle_x = -k_{\text{B}} \langle \ln p_i \rangle_x$$
$$\rightarrow \langle s \rangle_x = -k_{\text{B}} [x \ln(x) + (1 - x) \ln(1 - x)]. \tag{10}$$

It corresponds to the entropy terms of Eq. (4), when assuming in addition independent polaronic degrees of freedom with same x.

The equivalence of Eqs. (9) and (4) proves that the ideal mixing entropy should be used in combination with the mean-field averaged internal energy to obtain the exact mean-field approximation to the system under study. The long history and reliability of mean-field theories in physics indicates to us that this is the most straight forward way to derive the homogeneous free energy for phase field theories. In particular, no artificial length scales for determining averages at concentration x are introduced, as the average $\langle \tilde{u} \rangle_x = \frac{\langle U \rangle_x}{N}$ is purely based on the mean-field statistics, as defined in Eq. (8).

The internal energy average for a finite system with N potential Li lattice sites is given by

$$\langle \tilde{u} \rangle_x = \frac{1}{N} \sum_{\boldsymbol{\sigma}} p_x(\boldsymbol{\sigma}) U(\boldsymbol{\sigma}) \tag{11}$$

$$= \sum_{k=0}^{N} \sum_{(\sum \sigma_i = k)} x^k (1 - x)^{N-k} \frac{U(\boldsymbol{\sigma})}{N} \tag{12}$$

$$= \sum_{k=0}^{N} W(k, N, x) \cdot \langle \tilde{u} \rangle_{(k/N)}, \tag{13}$$

$$\langle \tilde{u} \rangle_{(k/N)} = \text{average at a concentration } k/N, \tag{14}$$

$$W(k, N, x) = \binom{N}{k} \cdot x^k (1 - x)^{N-k}. \tag{15}$$

For $N \rightarrow \infty : \langle \tilde{u} \rangle_x \rightarrow \langle \tilde{u} \rangle_{(k/N=x)}$. Therefore, in the limit of infinite simulation cell size, the average internal energy $\langle \tilde{u} \rangle_x$ approaches the trivial average of the internal energy over all states with global concentration x. All of these states have equal statistical weight. It should be stressed that the mean-field average is a nonthermodynamic average, e.g., low lying energetic states have no increased statistical weight due to a Boltzmann factor.

We test below two approaches (ii) and (iii) to calculate $\langle \tilde{u} \rangle_x$. In case (ii), we sample configuration space using the statistics given by formulas (13)–(15) and sampling within a $2 \times 2 \times 2$ supercell with 16 f.u.. In case (iii), we sample configuration space by the use of special quasi random structures (SQS) [70,71]. SQS are characterized by the exact properties given in Eqs. (6) and (7). Although used in many applications, to the best of our knowledge there are no publications that state explicitely that all quantities that are averaged using special quasi random structures are indeed averaged using the exact statistics of mean-field theory. Potential discrepancies in practice are due to imperfect sampling statistics with using a single SQS, that can only reproduce correct statistics for a limited number of interaction motives.

Having these limits of accuracy in mind, sampling and averaging the internal energy [Eqs. (13)–(15)] can as well be performed by evaluation of the energy of a representative SQS structure at x.

We start with construction scheme (i). In order to understand its accuracy we applied it first to $LiFePO_4$, the widely studied drosophila of phase separation, which allows a comparison to experimental, as well as to theoretical data. We determined defect energies within a $2 \times 2 \times 1$ supercell,

TABLE II. DFT derived open circuit voltages and internal energy parameters / defect energies $\bar{E}_d$ and δ (see text) for LFP. Solubility limits are derived from the free energy and are in perfect agreement with experimental values. The phase field theory parameters $\bar{E}_d$ of Ref. [39] were determined by a fit to experiments. $\Delta\mu_G$ is the estimated hysteretic gap as determined from the spinodal points of the constructed free energy.

	LFP	References
μ_{eq} vs Li(m) (eV)	−3.410	−3.47 [60]
$\bar{E}_d$, δ (eV)	0.174, −0.002	0.183 [26,39]
solubility limits (%)	4.6, 95.6	3.2, 96.2 [73]
$\Delta\mu_G$ (eV)	0.066	-

allowing atomic coordinates and the cell shape to relax while using the equivalent parameter set as within the materials project database [72]. As explained, the defect energies E_d^0 and E_d^1 are the energy of a single Li atom in the otherwise empty sublattice and the vacancy formation energy in the completely filled lattice at the equilibrium Li chemical potential μ_{eq}. As an example, E_d^0 is calculated via

$$E_d^0 = E^{DFT}(N(\mathrm{Li}) = 1) - E^{DFT}(N(\mathrm{Li}) = 0) - \mu_{eq}. \quad (16)$$

The results are presented in Table II. They allow direct determination of the free energy [Eq. (3) and (5)] and of the phase diagram of LFP by the common tangent construction. Indeed we find practically equivalent phase diagrams for LFP to the ones obtained by much more elaborate techniques or as in experiment. As an example, solubility limits at room temperature are in very good agreement with experiments (see Table II). Furthermore, the term $\bar{E}_d$ corresponds to the solid solution parameter used in phase field theory (as $\delta \approx 0$) models. With the defect energy method we find $\bar{E}_d =$ 0.174 eV, which agrees well with the commonly used phase field parameter of 0.183 eV, although the phase field theory parameters were determined by a fit to experiment [26,39]. These results indicate that our construction scheme yields reasonable homogeneous free energy values and is indeed a possible way for determining phase field parameters directly from rather simple ab-initio calculations. Other phase field simulations use slightly different values, which arises from the neglect of polaronic entropy effects in their model free energy [23].

For LFS, formation energies for interstitials and vacancies were calculated within a $2 \times 2 \times 2$ cell at μ_{eq}, allowing atomic coordinates and the cell shape to relax. We estimated the finite size errors to be of ≈20 meV which we ignore here. For construction schemes (ii) and (iii), we calculated the energies above hull for random structures in the same supercell. Averaged internal energies [Eq. (14)] were determined by averaging at concentrations k/N ($k = 1, \ldots, 15$, $N = 16$) before constructing the homogeneous MFT average according to Eq. (13) for intermediate concentrations x. The results are plotted in the upper part of Fig. 4, together with a fit of Eq. (5). The grey data points correspond to energies of randomly created structures, the green circles correspond to averages over the random structures [Eq. (14)] and the black solid line corresponds to the MFT average according to Eq. (13). The

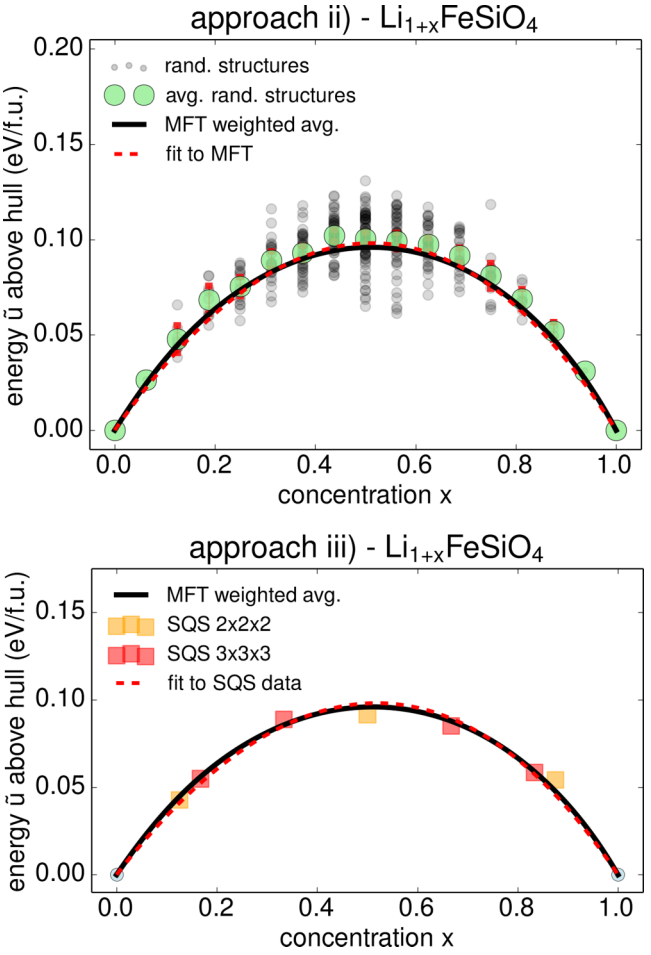

FIG. 4. Homogeneous sampling of the internal energy. (Top) Sampling according to approach (ii). Dark circles correspond to energies of individual random structures. Green circles correspond to averages over the random structures [Eq. (14)]. The black solid line corresponds to the MFT average according to Eq. (13), the red dashed line a fit of Eq. (5). (Bottom) Sampling according to approach (iii) using special quasi random structures in $2 \times 2 \times 2$ and in $3 \times 3 \times 3$ supercells, together with a fit and the MFT average determined in method (ii).

minute difference between the MFT average and the green datapoints suggests that the cell size is already close to the limiting value $N \to \infty$ where they are identical. We also want to point out that the black line is not a fit, but that the interpolation arises naturally from Eq. (13).

In addition, optimized SQS were constructed with the mcsqs tool of the ATAT software package [71,74–78] for concentrations $x = 0.25, 0.50, 0.75$ within the $2 \times 2 \times 2$ supercell and for concentrations $x = 1/6, 2/6, 4/6, 5/6$ within a $3 \times 3 \times 3$ supercell. The SQS were obtained by optimizing the correlation function match for pair, triple, and quadruple motives with a spatial extent of 7, 6, and 6 Å, respectively. The use of the bigger supercell was necessary to reduce correlation function mismatch for intermediate x. A perfect match was only obtained for $x = 0.5$. The resulting SQS energies are plotted in the lower part of Fig. 4 including the fit of Eq. (5) as red dashed line and the mean-field average from approach (ii) as black line. The equivalence of construction schemes (ii) and

TABLE III. DFT derived internal energy parameters/defect energies $\bar{E}_d$ and δ (see text) for LFS using the three different construction schemes. For methods (ii) and (iii), $\bar{E}_d$ and δ are found by a fit of Eq. (5) to the data (red dashed lines in Fig. 4). The open circuit voltage [μ_{eq}/e vs Li(m)] is −3.132 V.

LFS	approach		
	(i) defects	(ii) MFT avg.	(iii) SQS
$\bar{E}_d$, δ (eV)	0.461, −0.074	0.397, −0.041	0.399, −0.058
$\Delta\mu_G$ (eV)	0.522	0.412	0.414

(iii) is demonstrated by the practical equivalence of these lines as well as the free energy parameters as tabulated in Table III.

It furthermore indicates that the effective cluster interactions related to the considered correlation functions upon SQS construction include effectively all relevant interactions of the system. It should be noted, however, that the method here does not necessitate the construction of a cluster expansion, but is purely based on generating statistical samples of structures such that the distribution of correlation functions corresponds to the sampling probability given by mean-field theory.

Mean-field averaging [(ii) and (iii)] results in a noticeably lower interaction constant $\bar{E}_d$ for LFS when compared to the defect energy approach (i) (0.40 versus 0.46 eV, Table III). On the other hand, when comparing the order of magnitude, e.g., with respect to the LFP results (Table II), the difference seems less dramatic, in particular, if we are interested in comparing overall free energy shapes.

In a simplistic picture, e.g., if only homogeneous (de-)lithiation of battery particles is considered, the so-called hysteretic voltage gap $\Delta\mu_G$ [29,30] can be related to the shape of the underlying free energy, in particular the spinodal points. As a result it is possible to estimate $\Delta\mu_G$ directly from the interaction parameter $\bar{E}_d$. Under these assumptions we predict LFP to exhibit a smaller hysteretic voltage gap $\Delta\mu_G$ than LFS ($\Delta\mu_G = 0.07$ eV versus 0.52–0.41 eV, Tables II and III). The same observations are made indeed in experiment, however, with lower absolute values for both materials [30]. In reality, smaller gaps can be expected when nucleation happens. In order to study nucleation within phase field theory as in the case of LFP [24], elastic as well as interfacial energy terms need to be determined.

C. Elastic properties

Elastic constants for Li_1FeSiO_4 and Li_2FeSiO_4 were calculated by DFT within the $1 \times 1 \times 1$ primitive unit cell using two approaches. On the one hand relying on the VASP's internal routines, and on the other hand by fitting a quadratic energy expression according to linear elasticity [Eq. (17)] to appropriately deformed cells.

$$\Delta E = V\left(\sigma_{ik}\epsilon_{ik} + \tfrac{1}{2}C_{iklm}\epsilon_{ik}\epsilon_{lm}\right). \tag{17}$$

The relevant deformation gradient tensors $\bar{F}$ for orthorhombic cells were taken from Ref. [79]. $\bar{F}$ and the original and strained lattice vectors, represented by the cartesian row vectors of $\bar{b}_r$ and $\bar{B}_r$, respectively, are related by the following matrix multiplications:

$$\bar{B}_r = \bar{b}_r\bar{F}^\top, \quad \bar{F}^\top = \bar{b}_r^{-1}\bar{B}_r, \quad \bar{\epsilon} = \tfrac{1}{2}(\bar{F}^\top\bar{F} - \mathbf{1}). \tag{18}$$

We use the more general *Lagrangian* finite strain definition $\bar{\epsilon}$ in contrast to *infinitesimal* strains which erroneously do not vanish for infinitesimal rotations [80,81]. Furthermore we present results using the Voigt notation [82]. We applied deformations with strain components up to 7% and observed linear behavior. Indeed, the predicted energy of strained systems using Eq. (17) with the fitted constants was slightly more accurate than what Eq. (17) with VASP's elastic constants yields, which is why we report here the values fitted to explicit cell distortions. The elastic constants for $LiFeSiO_4$ and Li_2FeSiO_4 are tabulated in Table IV. In fact, $LiFeSiO_4$ (slightly nonorthorhombic) has nonorthorhombic tensor components with values <0.5 GPa, which allows to treat both materials as orthorhombic.

TABLE IV. Orthorhombic elastic constants of $Li_{1/2}FeSiO_4$ in Voigt notation [82].

C (GPa)	C_{11}	C_{22}	C_{33}	C_{44}	C_{55}	C_{66}	C_{12}	C_{13}	C_{23}
$LiFeSiO_4$	207	85	101	19	30	17	41	31	26
Li_2FeSiO_4	220	132	138	36	41	43	68	63	43

The elastic energy of strained precipitates in solids can be visualized by plotting $B(\mathbf{n})$, where $B(\mathbf{n})$ is given by [83]

$$\begin{aligned} B(\mathbf{n}) &= C_{ijkl}\epsilon^0_{ij}\epsilon^0_{kl} - n_i\sigma^0_{ij}\Omega_{jl}(\mathbf{n})\sigma^0_{lm}n_m, \\ [\Omega^{-1}]_{ij} &= C_{ikl\,j}n_k n_l, \\ \sigma^0_{ij} &= C_{ijkl}\epsilon^0_{kl}, \\ \text{with } \mathbf{n} &= \frac{\mathbf{k}}{|\mathbf{k}|}. \end{aligned} \tag{19}$$

We use the Einstein summation convention. $B(\mathbf{n})$ is a measure for the strain energy necessary to create a coherent interface perpendicular to the direction $\mathbf{n} = \mathbf{k}/k$. The terms contributing to $B(\mathbf{n})$ only depend on common elastic constants C_{ijkl} and the *stress free transformation strain* $\bar{\epsilon}^0$ which is the strain, necessary to transform the material with the host lattice constants to the precipitate equilibrium lattice constant. When the elastic constants of both phases differ significantly, an analysis of the strain energy is a little more involved [83–85]. Here we plot $B(\mathbf{n})$ for averaged elastic constants of both phases $LiFeSiO_4$ and Li_2FeSiO_4 and the values as in Tables IV and V. Figure 5 shows that the coherency strain energy is

TABLE V. Equilibrium unit cells and corresponding components of the related stress free transformation strain $\bar{\epsilon}^0$ for the nucleation of $LiFeSiO_4$ inside the Li_2FeSiO_4 matrix. Strain components are given in the Voigt notation.

	a (Å)	b (Å)	c (Å)	α	β	γ
$LiFeSiO_4$	6.091	5.622	5.044	90.0	90.8	90.0
Li_2FeSiO_4	6.332	5.395	4.998	90.0	90.0	90.0
	ϵ_1	ϵ_2	ϵ_3	ϵ_4	ϵ_5	ϵ_6
$\bar{\epsilon}^0$ (%)	−3.7614	4.4308	0.9236	−0.0005	−0.6538	−0.0021

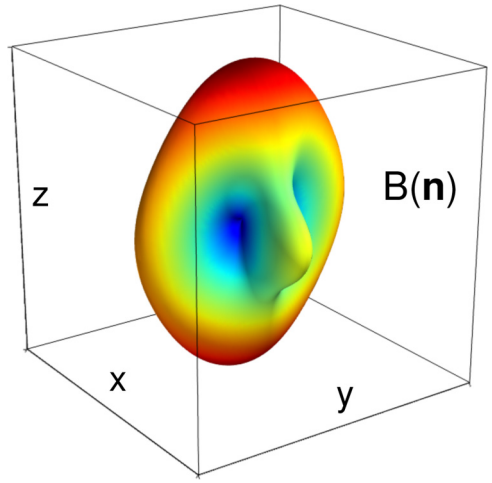

FIG. 5. $B(\mathbf{n})$ [Eq. (19)] for elastic constants corresponding to the average of $LiFeSiO_4$ and Li_2FeSiO_4. (x, y, z) is along the crystal axes (see Table V).

minimized along the ⟨110⟩ directions [(x, y, z) is along crystal axes, see Table V], which allow to conclude that large, strain energy dominated $LiFeSiO_4$ inclusions should be platelet-like and aligned approximately perpendicular to ⟨110⟩ (similar as in the case of LFP [23]).

D. Interface energies

Interface energies for (100), (010), (001), and (110) $LiFeSiO_4/Li_2FeSiO_4$ interfaces were determined from joining lattice-matched supercells of both phases along these directions. This implies that we restrict ourselves to atomically sharp interfacial structures. The studied heterostructures were thicker than 40 Å where the lattice constants of Li_2FeSiO_4 were used as common lattice parameters. For calculating interface energies, all atoms within the periodic heterostructures were allowed to relax, not however the supercell itself. In this case, the induced strain relaxation necessitates to correct appropriately the relevant bulk reference energies of the two phases by a correction term $\Delta E_s(\bar{B}_r)$ in order to obtain meaningfull and converging interface energies. We determine averaged interface energies according to the following formula:

$$\gamma(\bar{B}_r) = \frac{E_{\text{hetero}}(\bar{B}_r) - E_{\text{bulk}}(\bar{B}_r) + \Delta E_s(\bar{B}_r)}{2 \cdot A(\bar{B}_r)}. \quad (20)$$

Here, $\bar{B}_r$ is the common lattice (Li_2FeSiO_4). The exact procedure to determine, e.g., ΔE_s as well as a convergence study is discussed in detail in Ref. [63] to support the validity of this approach. As the lattice constants of $LiFeSiO_4$ and Li_2FeSiO_4 are practically identical, we expect our results to be hardly affected by the choice of the chosen common lattice. The obtained interface energies are tabulated in Table VI. Interface energies for arbitrary directions are interpolated by a fitted, ellipsoidal directional dependence of the following form:

$$\gamma(\theta, \phi) = \frac{1}{\sqrt{\frac{\sin^2(\theta)\cos^2(\phi)}{a^2} + \frac{\sin^2(\theta)\sin^2(\phi)}{b^2} + \frac{\cos^2(\theta)}{c^2}}}. \quad (21)$$

TABLE VI. DFT determined interface energies γ. We also included the semiaxes lengths a, b, and c along the Cartesian axes x, y, and z for a fitted, interpolating ellipsoid given by Eq. (21).

interface	(100)	(010)	(001)	(110)	a	b	c
γ (meV/Å^2)	11.6	8.9	7.1	10.5	11.77	9.37	7.10

We note in passing, that—due to the lack of data—we implicitly assumed a very smooth directional dependence with no energy extrema for intermediate directions which might, however, be existent in reality. The fitted values for a, b, and c are tabulated as well in Table VI, where a, b, and c are the semiaxes along the Cartesian axes x, y, and z and θ and ϕ the respective angles in spherical coordinates.

The determined interface energies are for atomically sharp interfaces. Within phase field theory, however, interface energy terms are represented by gradient terms of, e.g., a concentration field. In order to determine the interface term in Eq. (1) that goes along with the above proposed free energy density, we proceed by matching the total energy expression of a Cahn-Hilliard model to DFT results as follows.

$\Phi[x(\mathbf{r})]$ in Eq. (1) becomes stationary for equilibrium density profiles $x(\mathbf{r})$, as well as for critical nuclei, as elaborated in Refs. [31,32]. Just as a side remark, we want to stress that, in contrast to classical nucleation theory, this approach exhibits a more realistic behavior for large overpotentials and close to critical points (e.g., the spinodal), where nucleation barriers vanish as the homogeneous bulk free energy becomes unstable against infinitesimal density fluctuations, which cannot be properly described by classical nucleation theory.

We assume the scalar κ and the site density ρ to be concentration- and temperature-independent, in agreement with most phase field theory publications [23,24,26,34,36–39].

Here, $\phi(x(\mathbf{r}), T)$ at equilibrium chemical potential has been constructed before in this work [Eq. (4), $\delta\mu = 0$]. For simplicity, we restrict ourselves to a one parameter internal energy $\tilde{u}(x) = \bar{E}_d x(1-x)$, as in most phase field theory simulations. A refit results in $\bar{E}_d = 0.412$ eV. We estimate κ by requiring the 0-K interface energies for (atomically) sharp interfaces as from Table VI to correspond to the Cahn-Hilliard result at 0 K.

The atomically sharp interface, where the concentration varies from $x = 0$ to $x = 1$, is assumed to correspond within Cahn-Hilliard theory to a linear variation in x across an interface width given by the lattice parameter $a = 1/\sqrt[3]{\rho}$. The gradient $|\nabla x|$ reduces to $\frac{1}{a}$ and the interface energy σ can be expressed by a one-dimensional integral across the interface at the equilibrium chemical potential (see, e.g., Refs. [31,32]), which gives at 0 K:

$$\sigma = \rho \int_{-\infty}^{\infty} \left[\tilde{u}(x(r)) + \kappa \left(\frac{dx}{dr} \right)^2 \right] dr, \quad (22)$$

$$\sigma = \rho \left(\frac{a}{6} \bar{E}_d + \kappa \frac{1}{a} \right), \quad (23)$$

$$\kappa = a^4 \sigma - \frac{a^2}{6} \bar{E}_d. \quad (24)$$

TABLE VII. DFT determined parameters and the derived Cahn-Hilliard (CH) gradient penalty parameter κ.

	relevant CH parameters		
γ_0 (meV/Å^2)	a (Å)	$\bar{E}_d$ (meV)	κ_0 (meVÅ^2)
7.1	4.4	412	1338

We derive κ from the minimum of the determined interface energies γ_0 of atomically sharp interfaces by substituting the Cahn-Hilliard interface energy σ in Eq. (24) with the DFT-determined interface energy γ_0. The extension of Eqs. (22)–(24) towards tensorial κ for dealing with direction dependent interface energies is straight forward. The so-determined, relevant Cahn-Hilliard continuum parameters for LFS are tabulated in Table VII.

The (temperature dependent) Cahn-Hilliard equilibrium interface energy σ and width l for a phase-separated state, where both phases are in equilibrium, are derived in Ref. [31] and are given by

$$\sigma = 2\rho\sqrt{\kappa}\int_{x_0}^{x_1}\sqrt{\Delta\phi(x)}dx, \tag{25}$$

$$\Delta\phi(x) = \phi(x, T, \delta\mu = 0) - \phi(x_0, T, \delta\mu = 0), \tag{26}$$

$$x_{0,1} : \frac{\partial}{\partial x}\phi(x, T, \delta\mu = 0)|_{x_0,x_1} = 0, \tag{27}$$

$$l \approx (x_1 - x_0)\frac{\sqrt{\kappa}}{\sqrt{\Delta\phi(x = 0.5)}}. \tag{28}$$

After having parametrized the Cahn-Hilliard model from requiring it to reproduce the DFT interface energy using a nonequilibrium stepwise concentration profile, it is possible to find the equilibrium interface energy within the Cahn-Hilliard model for a range of temperatures different from 0.

The temperature dependence of interface widths l and interface energies σ are obtained by numerical solution of Eqs. (25)–(28) for $T = 0$–350 K and plotted in Fig. 6. Even at 0 K we observe a slight reduction of the interface energy due to the fact that the step wise assumed trial concentration profile was not a minimizing profile of the Cahn-Hilliard equation (7.1 versus 6.8 meV/Å^2).

Some interface broadening is expected for room temperature [l (0/300 K) = 3.6/4.5 Å]. It should be noted that the thicknesses l are only an estimate for the thickness of a smooth concentration variation across the interface. Yet it can be stated that the determined parameters indicate rather sharp interfaces of the size of one lattice constant, which is due to that fact that intermediate concentrations which arise for smeared out interfaces are energetically rather unfavourable for LFS (see Fig. 4). More interesting is the estimated temperature evolution of the interface energy, which becomes considerably lower as the calculated 0 K DFT value: $\gamma_0 = 7.1$ meV/Å^2 $\Leftrightarrow$ $\sigma(0/300\,\mathrm{K}) = 6.8/5.3$ meV/Å^2. This is ultimately related to the fact that the energy contributions of spacial regions with intermediate concentration become less with higher temperature, due to an increased stabilization of those.

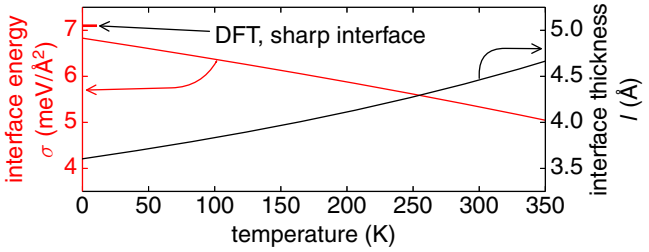

FIG. 6. Temperature dependence of the interface width l and interface energy σ as obtained from the *ab initio* parametrized Cahn-Hilliard model [Eqs. (25)–(28) for $T = 0$–350 K].

IV. DISCUSSION AND OUTLOOK

We have derived from *ab initio* calculations the relevant continuum parameters necessary for simulating the behavior of $Li_{1+x}FeSiO_4$ using phase field theory. This includes the nonconvex homogeneous bulk free energy density, the elastic and the interfacial energy terms. For the construction of the free energy density, we focused on rationalizing an appropriate way for determining the internal energy, given that it is combined with the common ideal solution entropy expression. The simplest construction scheme (i) is motivated by the fact that the lowest-order polynomial expressions for the internal energy that interpolates smoothly between the two limiting compositions can be related identically to defect energies, e.g., vacancies or interstitials. The accuracy of this approach was validated for Li_xFePO_4, by being able to reproduce experimental solubility limits and phase field parameters published in literature. In addition, we pointed out that a generic free energy expression with an ideal solution entropy part as, e.g., used in the CALPHAD approach and derived free energy expressions can be identified with the exact mean-field solution for lattice type systems. As a result, we suggested to combine the ideal solution entropy with an averaged internal energy, calculated using the sampling statistics of mean-field theory. Furthermore, the equivalence of mean-field sampling statistics and the statistics underlying the construction of special quasi random structures was highlighted, and exemplified by calculating the mean-field averaged and the SQS averaged internal energy of $Li_{1+x}FeSiO_4$.

We showed that it is possible to determine homogeneous free energy densities as used in phase field theory from a very reduced number of *ab initio* calculations, e.g., without the need of constructing a cluster expansion or similar approximations. In particular, we want to note that the nonconvex free energy expression by mean-field sampling is well-defined in the sense that it is independent of the sampled cell size, given a certain minimum size defined by the extent of the interactions.

Although being only an approximation, mean-field theory gives in many cases a very good qualitative and even quantitative agreement with the true solution of the problem, as exemplified by the three-dimensional Ising model. We showed here that derived solubility limits for LFP are in very good agreement with experiment and that mean-field derived estimated hysteretic voltage gaps of LFP and LFS show the correct trends when compared to experiment.

In addition we determined elastic properties and analyzed briefly the expected alignment of interfaces in phase

separated situations along the ⟨110⟩ directions. Furthermore, we determined interface energies using DFT and derived the corresponding interfacial penalty term for a phase field model of LFS.

To our knowledge, such a recipe for the determination of all relevant phase field parameters from *ab initio* calculations has not been put forward and applied before. In addition, the demonstrated relationship between mean-field free energies and semiempirical model free energies is important to understand the range of validity of past and future work in thermochemical modeling. As an example, the authors of Ref. [67] propose the "semiempirical" construction of phase-diagrams for pseudobinary systems based on combining the ideal mixing entropy with an internal energy averaged over highly symmetric structures (HSS). They tested this "semiempirical" approach by comparison to the correct phase diagrams obtained by Monte Carlo sampling. The theoretical assessment in this work here allows to evaluate this semiempirical approach and derive that it corresponds to a large extent to a mean-field free energy construction as the HSS-averaged internal energy corresponds approximately to the mean-field average. As a result, the equivalence of the HSS and Monte Carlo phase diagrams in Ref. [67] can be interpreted as a prove of the accuracy of mean-field theory. In addition, this hints towards the possibility of constructing in a very effective way approximate free energies, e.g., for phase diagrams in a high-throughput way, by the use of a few SQS computations.

In addition, we hope that the numerical results of this study will enable researchers in the battery community to simulate and understand better the behavior of LFS in particular in comparison to LFP. We will analyze different delithiation mechanisms of LFS in a follow up paper.

ACKNOWLEDGMENTS

We thank Nicola Marzari, Robert Baldock, and Clare Grey for helpful comments on this work.

[1] J. Sanchez, F. Ducastelle, and D. Gratias, Physica A **128**, 334 (1984).
[2] G. Ceder, Comput. Mater. Sci. **1**, 144 (1993).
[3] A. Van der Ven, J. C. Thomas, Q. Xu, and J. Bhattacharya, Math. Comput. Simulat. **80**, 1393 (2010).
[4] R. Malik, F. Zhou, and G. Ceder, Nat. Mater. **10**, 587 (2011).
[5] K. Persson, Y. Hinuma, Y. S. Meng, A. Van der Ven, and G. Ceder, Phys. Rev. B **82**, 125416 (2010).
[6] E. Lee and K. A. Persson, Chem. Mater. **25**, 2885 (2013).
[7] O. Penrose and P. C. Fife, Physica D **43**, 44 (1990).
[8] S.-L. Wang, R. Sekerka, A. Wheeler, B. Murray, S. Coriell, R. Braun, and G. McFadden, Physica D **69**, 189 (1993).
[9] A. Wheeler, B. Murray, and R. Schaefer, Physica D **66**, 243 (1993).
[10] H. Emmerich, Adv. Phys. **57**, 1 (2008).
[11] G. K. Singh, G. Ceder, and M. Z. Bazant, Electrochim. Acta **53**, 7599 (2008).
[12] D. A. Cogswell, Phys. Rev. E **92**, 011301(R) (2015).
[13] Y. S. Meng and M. E. Arroyo de Dompablo, Acc. Chem. Res. **46**, 1171 (2013).
[14] M. S. Islam and C. A. J. Fisher, Chem. Soc. Rev. **43**, 185 (2014).
[15] L. Suo, W. Han, X. Lu, L. Gu, Y.-S. Hu, H. Li, D. Chen, L. Chen, S. Tsukimoto, and Y. Ikuhara, Phys. Chem. Chem. Phys. **14**, 5363 (2012).
[16] C. Zhu, L. Gu, L. Suo, J. Popovic, H. Li, Y. Ikuhara, and J. Maier, Adv. Funct. Mater. **24**, 312 (2014).
[17] L. Gu, C. Zhu, H. Li, Y. Yu, C. Li, S. Tsukimoto, J. Maier, and Y. Ikuhara, J. Am. Chem. Soc. **133**, 4661 (2011).
[18] Y. Sun, X. Lu, R. Xiao, H. Li, and X. Huang, Chem. Mater. **24**, 4693 (2012).
[19] G. Chen, X. Song, and T. J. Richardson, Electrochem. Solid-State Lett. **9**, A295 (2006).
[20] N. Meethong, H.-Y. Huang, S. Speakman, W. Carter, and Y.-M. Chiang, Adv. Funct. Mater. **17**, 1115 (2007).
[21] A. Van der Ven, K. Garikipatib, S. Kimb, and M. Wagemaker, J. Electrochem. Soc. **156**, A949 (2009).
[22] M. Wagemaker, F. M. Mulder, and A. Van der Ven, Adv. Mater. **21**, 2703 (2009).
[23] D. A. Cogswell and M. Z. Bazant, ACS Nano **6**, 2215 (2012).
[24] D. A. Cogswell and M. Z. Bazant, Nano Lett. **13**, 3036 (2013).
[25] B. Orvananos, R. Malik, H.-C. Yu, A. Abdellahi, C. P. Grey, G. Ceder, and K. Thornton, Electrochim. Acta **137**, 245 (2014).
[26] M. J. Welland, D. Karpeyev, D. T. O'Connor, and O. Heinonen, ACS Nano **9**, 9757 (2015).
[27] R. Malik, D. Burch, M. Bazant, and G. Ceder, Nano Lett. **10**, 4123 (2010).
[28] R. Malik, A. Abdellahi, and G. Ceder, J. Electrochem. Soc. **160**, A3179 (2013).
[29] W. Dreyer, J. Jamnik, C. Guhlke, R. Huth, J. Moskon, and M. Gaberscek, Nat. Mater. **9**, 448 (2010).
[30] W. Dreyer, C. Guhlke, and R. Huth, Physica D **240**, 1008 (2011).
[31] J. W. Cahn and J. E. Hilliard, J. Chem. Phys. **28**, 258 (1958).
[32] J. W. Cahn and J. E. Hilliard, J. Chem. Phys. **31**, 688 (1959).
[33] D. W. Oxtoby, J. Phys.: Condens. Matter **4**, 7627 (1992).
[34] B. Han, A. V. der Ven, D. Morgan, and G. Ceder, Electrochim. Acta **49**, 4691 (2004).
[35] D. Burch and M. Z. Bazant, Nano Lett. **9**, 3795 (2009).
[36] Y.-H. Kao, M. Tang, N. Meethong, J. Bai, W. C. Carter, and Y.-M. Chiang, Chem. Mater. **22**, 5845 (2010).
[37] M. Tang, J. F. Belak, and M. R. Dorr, J. Phys. Chem. C **115**, 4922 (2011).
[38] M. Wagemaker, D. P. Singh, W. J. Borghols, U. Lafont, L. Haverkate, V. K. Peterson, and F. M. Mulder, J. Am. Chem. Soc. **133**, 10222 (2011).
[39] P. Bai, D. A. Cogswell, and M. Z. Bazant, Nano Lett. **11**, 4890 (2011).
[40] *CALPHAD: Calculation of Phase Diagrams A Comprehensive Guide*, edited by N. Saunders and A. P. Miodownik, Pergamon Materials Series Vol. 1 (Pergamon, Oxford, 1998).
[41] *Intermetallic Chemistry*, edited by R. Ferro and A. Saccone, Pergamon Materials Series Vol. 13 (Pergamon, Oxford, 2008), pp. 7–80.

[42] U. Grafe, B. Böttger, J. Tiaden, and S. Fries, Scr. Mater. **42**, 1179 (2000).
[43] J. Zhu, Z. Liu, V. Vaithyanathan, and L. Chen, Scr. Mater. **46**, 401 (2002).
[44] T. Kitashima, Philos. Mag. **88**, 1615 (2008).
[45] S. G. Fries, B. Boettger, J. Eiken, and I. Steinbach, Inter. J. Mater. Res., IJMR **100**, 128 (2009).
[46] I. Steinbach, B. Böttger, J. Eiken, N. Warnken, and S. G. Fries, J. Phase Equilib. Diffus. **28**, 101 (2007).
[47] R. Dominko, M. Bele, M. Gaberscek, A. Meden, M. Remskar, and J. Jamnik, Electrochem. Commun. **8**, 217 (2006).
[48] M. Arroyo de Dompablo, J. Gallardo-Amores, J. García-Martínez, E. Morán, J.-M. Tarascon, and M. Armand, Solid State Ionics **179**, 1758 (2008).
[49] M. S. Islam, Philos. Trans. R. Soc. London, Ser. A **368**, 3255 (2010).
[50] A. R. Armstrong, N. Kuganathan, M. S. Islam, and P. G. Bruce, J. Am. Chem. Soc. **133**, 13031 (2011).
[51] A. Saracibar, A. Van der Ven, and M. Arroyo de Dompablo, Chem. Mater. **24**, 495 (2012).
[52] N. G. Hörmann and A. Groß, J. Solid State Electrochem. **18**, 1401 (2014).
[53] G. Kresse and J. Furthmüller, Phys. Rev. B **54**, 11169 (1996).
[54] G. Kresse and J. Furthmüller, Comput. Mater. Sci. **6**, 15 (1996).
[55] P. E. Blöchl, Phys. Rev. B **50**, 17953 (1994).
[56] G. Kresse and D. Joubert, Phys. Rev. B **59**, 1758 (1999).
[57] N. G. Hörmann and A. Groß, Chem. Phys. Chem. **15**, 2058 (2014).
[58] J. P. Perdew, K. Burke, and M. Ernzerhof, Phys. Rev. Lett. **77**, 3865 (1996).
[59] S. L. Dudarev, G. A. Botton, S. Y. Savrasov, C. J. Humphreys, and A. P. Sutton, Phys. Rev. B **57**, 1505 (1998).
[60] F. Zhou, M. Cococcioni, C. A. Marianetti, D. Morgan, and G. Ceder, Phys. Rev. B **70**, 235121 (2004).
[61] M. Arroyo de Dompablo, M. Armand, J. Tarascon, and U. Amador, Electrochem. Commun. **8**, 1292 (2006).
[62] A. Kokalj, R. Dominko, G. Mali, A. Meden, M. Gaberscek, and J. Jamnik, Chem. Mater. **19**, 3633 (2007).
[63] See Supplemental Material at http://link.aps.org/supplemental/10.1103/PhysRevMaterials.3.055401 for details on the interface energy calculations.
[64] H. Fröhlich, Adv. Phys. **3**, 325 (1954).
[65] J. T. Devreese, arXiv:cond-mat/0004497 [cond-mat.str-el].
[66] F. Zhou, T. Maxisch, and G. Ceder, Phys. Rev. Lett. **97**, 155704 (2006).
[67] D. Usanmaz, P. Nath, J. J. Plata, G. L. W. Hart, I. Takeuchi, M. B. Nardelli, M. Fornari, and S. Curtarolo, Phys. Chem. Chem. Phys. **18**, 5005 (2016).
[68] W. L. Bragg and E. J. Williams, Proc. Royal Soc. London A: Math., Phys. and Engineering Sci. **145**, 699 (1934).
[69] M. Plischke and B. Bergersen, *Equilibrium Statistical Physics*, 3rd ed. (World Scientific, Singapore, 2006).
[70] A. Zunger, S.-H. Wei, L. G. Ferreira, and J. E. Bernard, Phys. Rev. Lett. **65**, 353 (1990).
[71] A. van de Walle, P. Tiwary, M. de Jong, D. Olmsted, M. Asta, A. Dick, D. Shin, Y. Wang, L.-Q. Chen, and Z.-K. Liu, Calphad **42**, 13 (2013).
[72] A. Jain, S. P. Ong, G. Hautier, W. Chen, W. D. Richards, S. Dacek, S. Cholia, D. Gunter, D. Skinner, G. Ceder, and K. A. Persson, APL Mater. **1**, 011002 (2013).
[73] A. Yamada, H. Koizumi, N. Sonoyama, and R. Kanno, Electrochem. Solid-State Lett. **8**, A409 (2005).
[74] A. van de Walle and G. Ceder, J. Phase Equilib. **23**, 348 (2002).
[75] A. van de Walle and M. Asta, Modell. Simul. Mater. Sci. Eng. **10**, 521 (2002).
[76] A. van de Walle, M. Asta, and G. Ceder, Calphad **26**, 539 (2002).
[77] G. L. W. Hart and R. W. Forcade, Phys. Rev. B **77**, 224115 (2008).
[78] A. van de Walle, Calphad **33**, 266 (2009), tools for Computational Thermodynamics.
[79] P. Ravindran, L. Fast, P. A. Korzhavyi, B. Johansson, J. Wills, and O. Eriksson, J. Appl. Phys. **84**, 4891 (1998).
[80] D. C. Wallace, *Thermodynamics of Crystals* (Wiley, New York, 1972), pp. XVIII, 484 S.
[81] *Mechanics of Solids, Volume II: Linear Theories of Elasticity and Thermoelasticity, Linear and Nonlinear Theories of Rods, Plates, and Shells*, edited by C. Truesdell (Springer-Verlag, Berlin, Heidelberg, 1972).
[82] P. Helnwein, Comput. Methods Appl. Mech. Eng. **190**, 2753 (2001).
[83] A. G. Khachaturiyan, *Theory of Structural Transformations in Solids* (Dover, Mineola, 2008).
[84] J. D. Eshelby, Proc. R. Soc. London, Ser. A **241**, 376 (1957).
[85] J. D. Eshelby, Proc. R. Soc. London, Ser. A **252**, 561 (1959).